Journal of Engineering Physics and Thermophysics, Vol. 79, No. 6, 2006

LASER DIGITAL SPECKLE ANEMOMETRY OF FLOWS IN MICROCHANNELS OF PEM FUEL CELLS

N. B. Bazylev, E. I. Lavinskaya, and N. A. Fomin

UDC 535.311 + 536.24

This paper considers the method of laser digital speckle anemometry and the software developed on its basis which make it possible to recover up to 250,000 velocity vectors in the two-dimensional region of the flow in a microchannel of size 20 × 30 mm in photography with optical magnification $\mathfrak{M} = 1$. The results of the investigations confirm the high temporal and spatial resolution of the proposed technique and point to its possible realization in real time. In the configuration presented the spatial resolution in the measurement plane is about 100 μm. It has been shown that experimental noise filtering is an important part of the analysis.

Introduction. One major problem in upgrading the efficiency of modern fuel cells is the provision of optimal conditions for feeding components and distributing them over the surface of the polymer electrolyte membrane (PEM) under the conditions of conversion of released energy of plasma-chemical reactions to useful electric energy (see Fig. 1) [1, 2]. It is transparent for protons and opaque for electrons, thus providing an electron flow in the external circuit, as shown in Fig. 1. The acronym PEM is also used for as Proton Exchange Membrane. Quantitative visualization of flows needed for such optimization is difficult in investigating processes under the conditions of internal microchannels with characteristic dimensions of 1 mm and less. The classical methods of investigating electrochemical flows such as the electrochemical impedance method and the electrodiffusion method permit obtaining important information on the processes in a wall-adjacent flow with a high spatial resolution only at its individual points [3–5]. Therefore, optical visualization techniques that permit simultaneous obtaining of information about the whole of the flow field are still attractive [6–10].

One of the most developed methods of quantitative anemometry of flows is the so-called PIV method (particle image velocimetry — anemometry by analyzing images of visualizing particles) based on the statistical analysis of images of particles added to the flow. This technique was developed within the framework of holography and coherent speckle photography. Its first description appeared in 1977 and initially it was called speckle anemometry, anemometry in scattered (coherent) radiation, or simply speckle photography (see, e.g., [11–14]). The main disadvantage of the first speckle velocimeters was the two-stage character of the process inherent in all holographic methods: upon obtaining and "wet" development of a specklogram (hologram) its subsequent processing was carried out on a separate facility performing optical Fourier transformation [15]. The switch to digital laser technologies of direct input of high-resolution images into a personal computer (PC) and the possibility of their real-time analysis eliminated this disadvantage and considerably widened the possibilities of this technique [16–21]. The traditional difficulties of microflow diagnostics, which also remain in using the new methods of digital laser anemometry called DPIV (Digital PIV — digital (laser) anemometry by analyzing images of visualizing particles), are organization of optical access to the channel, formation of laser illumination, and selection of visualizing particles in investigating flows in microchannels (μ-PIV) [22, 23]. To solve these problems, at the Heat and Mass Transfer Institute of NAS of Belarus jointly with the laboratory of investigations of thermal processes of the University of Poitiers (France) a number of experimental models of fuel elements providing optical measurements on both cold and hot models have been developed. This paper presents the results of the quantitative anemometry of the flow in microchannels of the cold model of a fuel cell (see Fig. 2). The data have been obtained by the single-exposure PIV method developed by the authors which is based on autocorrelation analysis of the speckle fields generated under probing laser radiation scattering by the microspheres visualizing the flow.

A. V. Luikov Heat and Mass Transfer Institute, National Academy of Sciences of Belarus, 15 P. Brovka Str., Minsk, 220072, Belarus; e-mail: fomin@hmti.ac.by. Translated from Inzhenerno-Fizicheskii Zhurnal, Vol. 79, No. 6, pp. 176–189, November–December, 2006. Original article submitted February 9, 2006.

 1062-0125/06/7906-1230

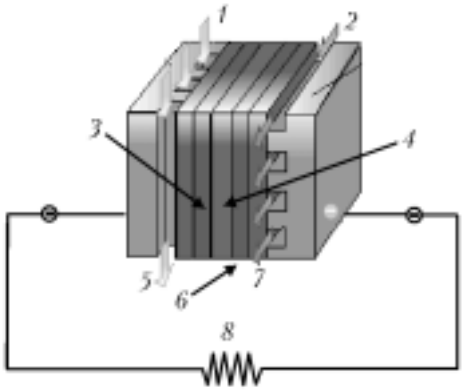

Fig. 1. Geometry of the PEM fuel element cells in the assemblage: 1) fuel (hydrogen) supply; 2) oxidizer (air or oxygen) supply; 3) anode with a platinum catalyzer causing decomposition of oxygen into positively charged ions (protons) and electrons; 4) PEM membrane passing only positively charged ions; 5) water formed on the cathode as a result of the recombination of charged reaction products; 6) cathode; 7) outlet of unused oxidizer; 8) useful load.

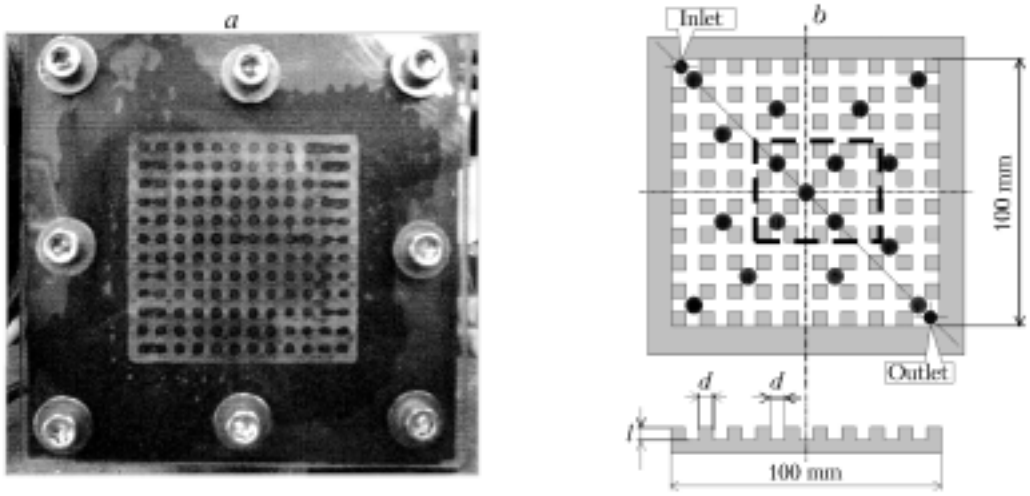

Fig. 2. Photograph of the cold fuel cell model with a transparent wall (a) and geometry of channels (b). Dots denote the arrangement of electrodiffusion sensors [4].

Experimental. The laser speckle anemometry used in the present work is based on statistical analysis of displacements of images of particles visualizing the flow being investigated in a finite time interval with digital recording of these particles in a selected plane by means of a CCD camera, as shown in Fig. 3a. Statistical averaging is made over a small zone of the CCD matrix containing a sufficient number of recording working cells (pixels), and in each chamber pixel the image is formed as a result of the total scattering in the volume given in Fig. 3a by the particles visualizing the flow into the solid angle Ω. Obviously, these particles should be uniformly introduced into the flow being investigated. For the particle velocities to completely "follow" the flow, they should be small enough. Usually, as in Doppler meters, these particles are of micron or even submicron size [24, 25].

It is usually impossible to organize laser illumination in microchannels exactly as shown in Fig. 3a because of the smallness of the channels and their complex configuration. In the present work, the microchannels were illuminated by collimated laser radiation just as in the case of anemometry in the near-surface blood flow in biotissue microcapillaries [26–31]. In so doing, as in biotissues, the influence of the multiple scattering effects leading to a faster transition from images of visualizing particles to speckle fields increases, and averaging of the information obtained over the channel depth (z-axis) occurs [32].

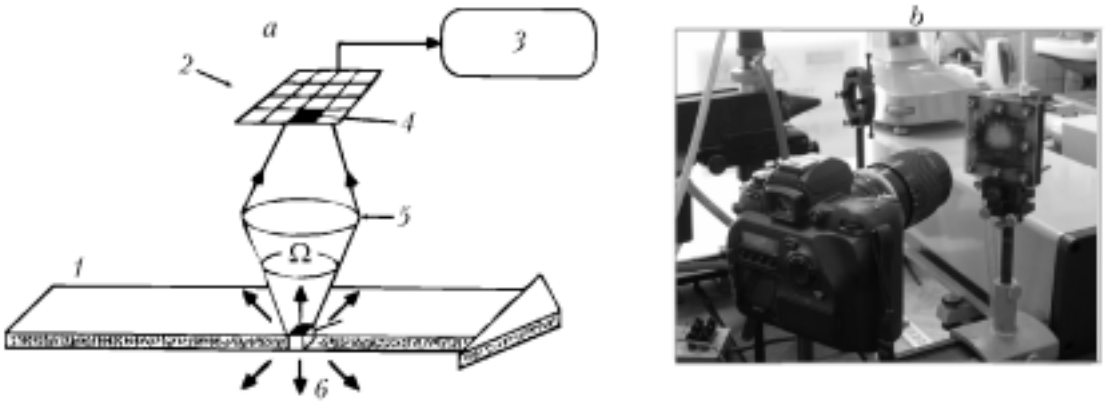

Fig. 3. Digital speckle field recorder: a) basic diagram of the recorder [1) "laser plane" for illumination; 2) CCD matrix element; 3) personal computer; 4) working cell (pixel); 5) focusing optics; 6) scattering volume)]; b) photograph of the recorder. The camera is focused on a semi-transparent model of the fuel cell.

The spatial resolution of anemometry is determined by the resolution of the receiving matrix and the sizes of the so-called averaging windows (zones) for which primary statistical analysis of measurement data is performed. Qualitative processing of specklograms requires comparatively large averaging windows, especially for cross-correlation analysis of images at large shifts between exposures. Thus, the analysis performed in [33] shows that the rms error in determining the sought shift of the speckle field decreases by a factor of 2–3 when the window size is changed from 32^2 to 128^2. Of course, such an increase in the size of averaging windows leads to considerable losses in the spatial resolution. Accordingly, a decrease in the window size from 32^2 to 16^2 leads to an increase in the errors by a factor of 2–3, but they can still be minimized to values of the order of 0.1 if all the other measurement parameters are optimized [9]. The use of such a window for a Fuji FinePix S2Pro matrix containing 4256 × 2848 pixels at $\mathfrak{M} = 1$ and overlap of windows of 0.5 provides a limiting spatial resolution of the order of 50 μm throughout the 20 × 30 mm field. A further decrease in the window size without loss of accuracy of statistical processing is only possible in special cases. For instance, in particular, for autocorrelation analysis in the one-exposure scheme the window size can be smaller, up to 5 × 5 or 7 × 7 pixels [28, 29].

Importantly, in the μ-PIV technique, the spatial resolution can be increased appreciably by decreasing the dimension of the investigated flow and increasing the number $\mathfrak{M}$. For instance, in the works of Prof. Meinhart [34, 35], an optical magnification $\mathfrak{M} = 100$ realized by means of a Nikon microscope, model ECLPSE E600FN, was used. Such an optical configuration permitted obtaining an image of a 415 × 415 μm flow with a spatial resolution of about 5 μm^2 even on a relatively small matrix of 1280 × 1024 pixels. In so doing, visualizing microparticles of diameter about 1 μm were used. A small further increase in the spatial resolution is possible at a smaller overlap of averaging windows (up to 0.25), which makes it possible to increase the number of velocity vectors being determined by a factor of 1.5–2.

The temporal resolution of recording velocity fields is determined by both the measuring circuit and the technical characteristics of the camera and the processor. In using the two-exposure scheme, the velocity field is determined as a result of the statistical analysis of the shifts of the images of visualizing particles in the time interval between successive frames obtained for exposures shorter than the process used. In this case, the time resolution is determined by the minimum time interval between successive frames, and in realizing continuous velocity monitoring — by the repetition frequency of recording image pairs and the time of cross-correlation analysis on the PC. The single-exposure technique uses a prolonged exposure time, during which the particles are noticeably shifted in the plane of images, and the autocorrelation analysis of these images permits determining the shift in the exposure time. In this case, the temporal resolution of the technique is determined by the minimum exposure time which is much shorter than the time interval between successive frames. In investigating ultrafast processes, the temporal resolution in this scheme can be improved in recording with an open shutter and exposure time control by regulating the laser

radiation duration. The exposure time in using the shutter of the given CCD camera can be varied from a few seconds to 250 μsec.

Such a principle of measurements was used for the first time in [26] in investigating the coronary blood flow and then developed sequentially for investigating the blood microcirculation [27–32] and laminar [36] and turbulent [36–38] flows. The single-composure speckle photography method is essentially a digital analog with statistical processing of the tracer method widely used in visualization [39]. Various combinations of this method with PIV and speckle photography techniques were used successfully in diagnosing microdisplacements in mechanics [40] and botany [41, 42].

Visualizing particles in the μ-DVIP technique largely determine the accuracy and even reliability of measurements. As mentioned above, they should, first of all, be small enough to completely follow the flow. In the μ-DVIP technique, the influence of velocity gradients on the lag of particles is usually weak, since the choice of the particle diameter d_p is also determined by the channel dimensions. At the same time the registered intensity of the scattered signal is proportional to the squared ratio of the particle diameter to the probing radiation wavelength $(d_p/\lambda)^2$. Therefore, the number of particles in the scattering volume and their diameter should be consistent with the laser power and the KCD camera sensitivity. Numerical simulation [11] shows that errors in the statistical determination of image shifts turn out to be minimum at image dimensions $d_s = (1.5–2.5)/d_{px}$. The dimensions of particle images with allowance for the diffraction effects are given by the relation $d_s = \sqrt{(\mathfrak{M} d_p)^2 + d_{dif}^2}$, where the diffraction component is defined as the Airy disc of the imaging system: $d_{dif} = 2.44(\mathfrak{M} + 1)\lambda F/D_L$. For $d_{px} \approx 10$ μm and $\mathfrak{M} = 1$ the optimum size of the visualizing particle $d_p = 5$ μm. The number of visualizing particles in a unit volume is also an important parameter in the statistical processing of the signal. The calculations [11] show that statistical errors in calculating a shift decrease from $0.08d_{px}$ for 16^2 particles per integration window to $0.01d_{px}$ for 64^2 particles. Under the conditions of the fuel element microchannel geometry this corresponds to the range from 25,000 to 400,000 particles/mm^3. The minimum quantity for the chosen diameter d_p is, in our opinion, a density of about 5000–10,000 particles/mm^3, which corresponds to 50–100 particles per integration window. Note that in dense suspensions these values are much higher. For instance, blood contains over 5 million erythrocytes/mm^3 at an erythrocyte size comparable to the chosen d_p.

In the present work, along with DANTEC visualizing powders, we also used microparticles representing hollow glass spheres of diameter about 5 μm. The spheres were made by an original technology at the Heat and Mass Transfer Institute of the NAS of Belarus with the use of plasmatrons and had an effective density of about 0.23 g/cm^3. Depending on the number of particles in a unit volume in the recording plane the scattered radiation forms either images of individual particles or speckle fields, while in digital recording of particles whose sizes are close to the sizes of pixels these notions become difficult to distinguish.

Statistical Analysis of the Data Obtained. The conventional algorithm of processing successive images with intensity distributions I_1, I_2 in their digital recording is given in Fig. 4. The sought shift of particles in each singled-out averaging window is determined by calculating the two-dimensional cross-correlation function of these images, also called specklograms. To this end, the obtained image is broken up into small subregions (averaging windows), in each of which the cross-correlation function is calculated depending on the coordinates of this subregion (m, n). With regard for the experimental noise in each zone of the specklogram $\tilde{\sigma}(m, n)$ the cross-correlation function represents the convolution of intensity distributions in the corresponding regions of the images being analyzed:

$$\mathbb{R}_{1,2}(m, n) = I_1(m, n) \otimes I_2^*(m, n) + \tilde{\sigma}(m, n) . \quad (1)$$

The transition to the Fourier plane [43] where this relation is of the form

$$\mathbb{F}\left\{\mathbb{R}_{1,2}\right\}(u, v) = \mathbb{F}\left\{I_1\right\}(u, v) \cdot \mathbb{F}\left\{I_2^*\right\}(u, v) + \sigma(u, v) \quad (2)$$

turns out to be convenient for analysis. Note that the Fourier transform of the specklogram with the speckle field intensity $I = I_1 + I_2$, as in two-exposure holographic speckle photography, represents a diffraction halo modulated by the well-known Young fringes, by the distance between which the averaged shift of speckles is determined in photographic

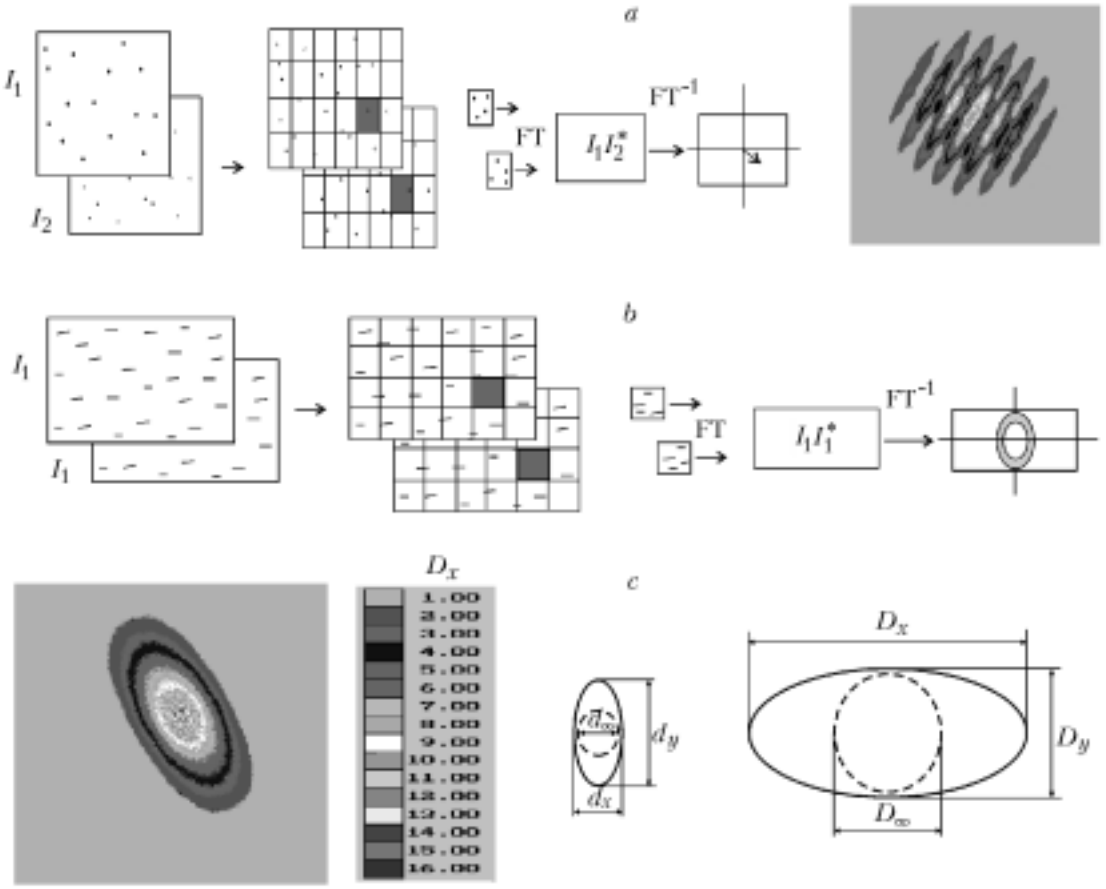

Fig. 4. Illustration of the cross-correlation analysis of a succession of images with the use of fast Fourier transform and PC-synthesized Fourier image of a specklogram with a speckle field intensity $I = I_1 + I_2$ (on the right) (a); illustration of the algorithm of autocorrelation analysis of a single-exposure specklogram with the use of fast Fourier transform (b); PC-synthesized diffraction halo of a single-exposure specklogram and main designations used in its analysis (c) (FT and FT* — direct and inverse Fourier transforms, respectively).

recording of specklograms and their optical processing by means of point-by-point scanning by a nondecollimated laser beam [15]:

$$\mathbb{F}\left\{I_1 + I_2\right\}(u, v) = \mathfrak{A}(u, v)\,. \tag{3}$$

The strategy of cross-correlation analysis of a succession of images consists of seeking the desired function $\mathbb{R}_{1,2}(m, n)$ by filtering the specklogram noise in both the initial physical plane and the Fourier plane for each subregion of images with intensities $I_1(m, n)$ and $I_2(m, n)$ (see Fig. 4a). An estimate of the sought function can be obtained in view of relation (2):

$$\tilde{\mathbb{R}}_{1,2}(m, n) = \mathbb{F}^{-1}\left\{\mathbb{F}\left\{\tilde{I}_1\right\}(u, v)\cdot\mathbb{F}\left\{\tilde{I}_2^*\right\}(u, v)\right\}, \tag{4}$$

where $\tilde{I}_1$, $\tilde{I}_2$ are the filtered intensity distributions in the specklograms. Below some methods of such filtering will be shown. Note that the cross-correlation functions $\tilde{\mathbb{R}}_{1,2}(m, n)$ and $\mathbb{R}_{1,2}(m, n)$ can also be calculated by direct comparison of corresponding images in all "pixels" of the CCD camera:

$$\mathbb{R}_{1,2}(m, n) = \frac{MN}{(M-m)(N-n)} \left[\frac{\sum_{p=1}^{M-m} \sum_{q=1}^{N-n} I_1(p, q) I_2(m+p, n+q)}{\sum_{p=1}^{M} \sum_{q=1}^{N} I_1(p, q) I_2(p, q)} \right]. \quad (5)$$

In not too highly noise-polluted regions, this function has a pronounced principal maximum at $m = m^*$ and $n = n^*$. Exactly these coordinates (m^*, n^*) determine the subregion-averaged value of the particle displacement in values of the pixel size d_{px}. Thus, the displacement vector magnitude can be calculated by the simple relation $\sqrt{\Delta \mathbf{d}^2} = d_{px}\mathfrak{M}\sqrt{(m^*)^2 + (n^*)^2}$. Because of the statistical character of calculations by relations (1)–(4) and natural filtering in averaging over large experimental data arrays the sought displacement value $\Delta^2 = (m^*)^2 + (n^*)^2$ is calculated with a very high (subpixel) accuracy even for highly noise-polluted flows, which permits quantitative determination of the two-dimensional velocity field with a high spatial resolution defined by a large number of flow points at which the velocity vector has been calculated.

In the μ-DPIV schemes it is not always possible to register the particle distribution in the image plane at the moments of two short exposures, as described above. At an exposure comparable to the characteristic time of the process under investigation the image of particles "blurs," the image contrast drops, and the value of this drop is directly proportional to the local velocity of particles in the investigated flow (see Fig. 4b). In this case, it is more convenient to analyze the specklogram obtained with the use of the autocorrelation functions

$$\mathfrak{J}_{1,1}(m, n) = I_1(m, n) \otimes I_1^*(m, n) + \tilde{\sigma}(m, n). \quad (6)$$

Here an analog of relation (2) will be

$$\mathbb{F}\left\{\mathfrak{J}_{1,1}\right\}(u, v) = \mathbb{F}\left\{I_1\right\}(u, v) \cdot \mathbb{F}\left\{I_1^*\right\}(u, v) + \sigma(u, v), \quad (7)$$

and an estimate of the sought autocorrelation function $\mathfrak{J}_{1,1}$ can be obtained using the relation

$$\mathfrak{J}_{1,1}(m, n) = \mathbb{F}^{-1}\left\{\mathbb{F}\left\{\tilde{I}_1\right\}(u, v) \cdot \mathbb{F}\left\{\tilde{I}_1^*\right\}(u, v)\right\}. \quad (8)$$

Evidently, this function $\mathfrak{J}_{1,1}(m, n)$ and its estimate $\tilde{\mathfrak{J}}_{1,1}(m, n)$ can also be calculated by direct comparison of the corresponding intensities analogously to (4):

$$\mathfrak{J}_{1,1}(m, n) = \frac{MN}{(M-m)(N-n)} \left[\frac{\sum_{p=1}^{M-m} \sum_{q=1}^{N-n} I_1(p, q) I_1(m+p, n+q)}{\sum_{p=1}^{M} \sum_{q=1}^{N} I_1(p, q) I_1(p, q)} \right]. \quad (9)$$

The Fourier transform of the one-exposure specklogram also represents a diffraction halo formed behind the specklogram upon its scanning by a laser beam. In this case, however, the halo is not modulated by interference fringes and represents a circle for a perfect speckle field recorded with the use of a short exposure or an ellipse with the semimajor axis direction orthogonal to the direction of the dominant displacement of speckles in the process of exposure whose duration is comparable to the characteristic time of the investigated process (see Fig. 4c). The fringes on the halo shown on the left in Fig. 4c result from the "quasi-color" representation of the elliptic distribution. Analogous fringes can also be noticed on real Young interference fringes with a "quasi-color" representation of the diffraction halo (see Fig. 4a, on the right).

The measured parameters in each window of the specklogram are the semiaxes of the diffraction halo ellipse D_x, D_y. As mentioned above, these quantities, and more precisely, their differences from the diameter of the initial speckle field diffraction halo D_∞ are proportional to the window-averaged increase in the dimensions (extension) of speckles along the corresponding orthogonal axes ($\langle \Delta d_x \rangle = \langle d_x - d_\infty \rangle$, $\langle \Delta d_y \rangle = \langle d_y - d_\infty \rangle$:

$$\frac{D_\infty (m, n)}{D_x (m, n)} = C_1 \frac{\langle d_x \rangle (m, n)}{\langle d_\infty \rangle (m, n)} = C_1 \frac{\langle \Delta d_x \rangle (m, n) + \langle d_\infty \rangle (m, n)}{\langle d_\infty \rangle (m, n)}, \tag{10}$$

$$\frac{D_\infty (m, n)}{D_y (m, n)} = C_1 \frac{\langle d_y \rangle (m, n)}{\langle d_\infty \rangle (m, n)} = C_1 \frac{\langle \Delta d_y \rangle (m, n) + \langle d_\infty \rangle (m, n)}{\langle d_\infty \rangle (m, n)}. \tag{11}$$

The coefficient C_1 in these relations can be assumed to be equal to 1. The extension of speckles in recording in a finite time interval Δt is determined by the measured velocity components V_x, V_y and by the optical magnification factor in specklogram recording $\mathfrak{M}$:

$$\Delta d_x = \mathfrak{M} V_x \Delta t, \quad \Delta d_y = \mathfrak{M} V_y \Delta t. \tag{12}$$

Thus, the sought velocity value turns out to be directly proportional to the relative decrease in the diffraction halo diameter with coefficient C_2, which, generally speaking, does not require dynamic calibration:

$$V_x = \frac{1}{C_1 \mathfrak{M} \Delta t} \frac{D_\infty - D_x}{D_x} = C_2 \frac{D_\infty - D_x}{D_x}, \tag{13}$$

$$V_y = \frac{1}{C_1 \mathfrak{M} \Delta t} \frac{D_\infty - D_y}{D_y} = C_2 \frac{D_\infty - D_y}{D_y}. \tag{14}$$

Another measured parameter of the one-exposure specklogram is the speckle field contrast. The contrast is different in different subregions of the specklogram and turns out to be inversely proportional to the particle velocity at the corresponding point of the flow at the moment of exposure. It can be determined by direct calculation by the formula

$$\mathbb{C}_{1,1} (m, n) = \frac{\sigma_{I_1} (m, n)}{\langle I_1 (m, n) \rangle} = \frac{\sqrt{\langle I (m, n)_1^2 \rangle - \langle I_1 (m, n) \rangle^2}}{\langle I_1 (m, n) \rangle} =$$

$$= \sqrt{\frac{1}{MN} \sum_{p=1}^{M} \sum_{q=1}^{N} \left[I_1^{m,n} (p, q) \right]^2 - \left[\frac{1}{MN} \sum_{p=1}^{M} \sum_{q=1}^{N} I_1^{m,n} (p, q) \right]^2} \Big/ \frac{1}{MN} \sum_{p=1}^{M} \sum_{q=1}^{N} I_1^{m,n} (p, q). \tag{15}$$

In a perfect speckle field, the value of $\sigma_{I_1}(m, n)$ is equal to the mean field intensity $\sigma_{I_1}(m, n) = \langle I_1(m, n) \rangle$, and the contrast $\mathbb{C}_{1,1}(m, n) = 1$. When the statistics is disturbed, e.g., due to the displacement of speckles during the exposure, the field contrast changes and one can determine by this contrast the velocity of scattering particles. Thus, in investigating the blood microcirculation, Prof. Briers obtained the following simplified relation relating the speckle field contrast to the speckle field correlation time τ_c depending on the velocity of scattering particles:

$$\mathbb{C}_{1,1} = \left\{ \frac{\tau_a}{2T} \left[1 - \exp (-2T/\tau_{\tilde{n}}) \right] \right\}^{1/2}. \tag{16}$$

The most general way of describing the space-time variations in speckle fields is the use of the space-time correlation formulas. In the normalized form for the fluctuating component $\Delta I = I - \langle I \rangle$ of the radiation intensity in the speckle field this function can be represented by the coefficient $\gamma_{\Delta I}$:

$$\gamma_{\Delta I}(\mathbf{r}_1, \mathbf{r}_2; t_1, t_2) = \frac{\langle \Delta I(\mathbf{r}_1, t_1)\, \Delta I(\mathbf{r}_2, t_2) \rangle}{\langle \Delta I(\mathbf{r}_1, t_1) \rangle\, \langle \Delta I(\mathbf{r}_2, t_2) \rangle}. \tag{17}$$

This quantity characterizes the mutual correlation of two fields obtained at different points in the space and at different instants of time and varies over the 0–1 range. Two methods for changing speckle fields are distinguished: speckle field "displacement," when some aggregation of speckles is displaced as a whole without changing their relative position, and "boiling" of speckles, when individual speckles appear and disappear chaotically at the same points in the space without experiencing noticeable displacements. Function (17) depends on many factors. One of the most important factors is the form of the laser beam generating the speckle field. For the Gaussian form of the beam when it is focused on the surface near the diffusing screen the spot diameter ω and the wave-front curvature ρ are given as a function of the distance z from the position of the beam waist

$$\omega = \omega_0 \left[1 + \left(\frac{z}{z_0} \right)^2 \right]^{\frac{1}{2}}, \quad \rho = z \left[1 + \left(\frac{z}{z_0} \right)^2 \right]^{\frac{1}{2}}, \tag{18}$$

where $z_0 = \pi\omega_0^2/\lambda$. The correlation time τ_c and the delay time τ_d were introduced in [44] to describe the dynamic properties of speckle fields experiencing simultaneously two modes of change — "displacement" and "boiling":

$$\gamma_{\Delta I}(\mathbf{r}, \tau) = \exp\left(-\frac{|\mathbf{r}|^2}{r_{\tilde{n}}^2} \right) \exp\left[-\frac{(\tau - \tau_d)^2}{\tau_{\tilde{n}}^2} \right], \tag{19}$$

where $\mathbf{r} = \mathbf{r}_2 - \mathbf{r}_1$, $\tau = t_2 - t_1$, and the delay time τ_d depends on $\mathbf{r}$.

Calculations of the correlation functions and the contrast of speckle fields on modern PCs can be made in the time interval between successive frames in recording digital images in the television standard (at a frequency of 25 Hz this interval is 40 msec) even for CCD cameras of limiting high resolution, which permits constructing systems of real-time diagnostics.

Dynamic Calibration of the One-Exposure Scheme of Speckle Anemometry of Microflows. The two-exposure scheme of PIV does not require calibration, since the integration-window-averaged velocity vector $\langle \mathbf{V} \rangle$ is defined by the simple relation $\langle \mathbf{V} \rangle = \langle \mathbf{\Delta d} \rangle / dt$, where the averaged displacement vector of the speckle field $\langle \mathbf{\Delta d} \rangle$ is measured in units of the dimension of the elementary pixel of the CCD matrix (known quantity), and the time interval between frames — in seconds.

In the above one-exposure scheme, the measured parameter is the window-averaged relative increase in the dimension (extension) of speckles at a comparatively prolonged exposure $\langle \Delta d_x \rangle / \langle d_\infty \rangle$, $\langle \Delta d_y \rangle / \langle d_\infty \rangle$. Therefore, for absolute measurement of the quantities $\langle \Delta d_x \rangle$, $\langle \Delta d_y \rangle$ independent determination of the average size of speckles $\langle d_\infty \rangle$ at a short exposure is needed. Such measurement can be made by means of autocorrelation analysis of the specklogram of the static speckle field. In the present work, the operating capacity of the one-exposure scheme and its dynamic calibration were tested in recording moving speckle fields generated by a rotating disc made of matte glass (see Fig. 5). The exposure time was chosen so that the relative extension of speckles varied from 0.1 in the central region of the disc to 5–10 at its periphery.

Figure 6 shows the evolution of the autocorrelation function of the specklogram of a rotating disc as the averaging window was moving from the center of the disc to its periphery. The obtained velocity profile for the rotating disc is linear to a fair accuracy, which conforms to the chosen model of motion. Velocity measurements are taken simultaneously at 88 points ("subzones"), which permits simultaneous obtaining of two-dimensional information throughout the flow field. The calibration results presented in Fig. 7 show that the velocity dependence of the relative extension of speckles is practically linear in the range of $\Delta d / d_\infty = 0.25$–5, which corresponds to the dynamic range of

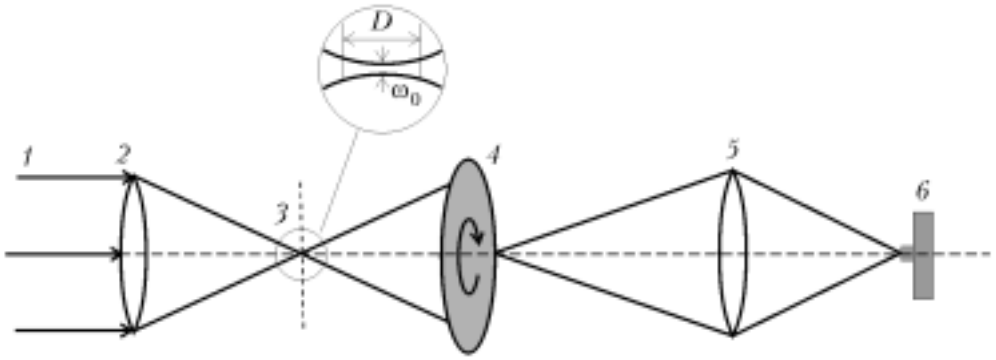

Fig. 5. Scheme of calibration with a rotating optical disc: 1) collimated laser radiation; 2) waist-forming lens; 3) waist position; 4) rotating disc; 5) imaging lens; 6) CCD camera.

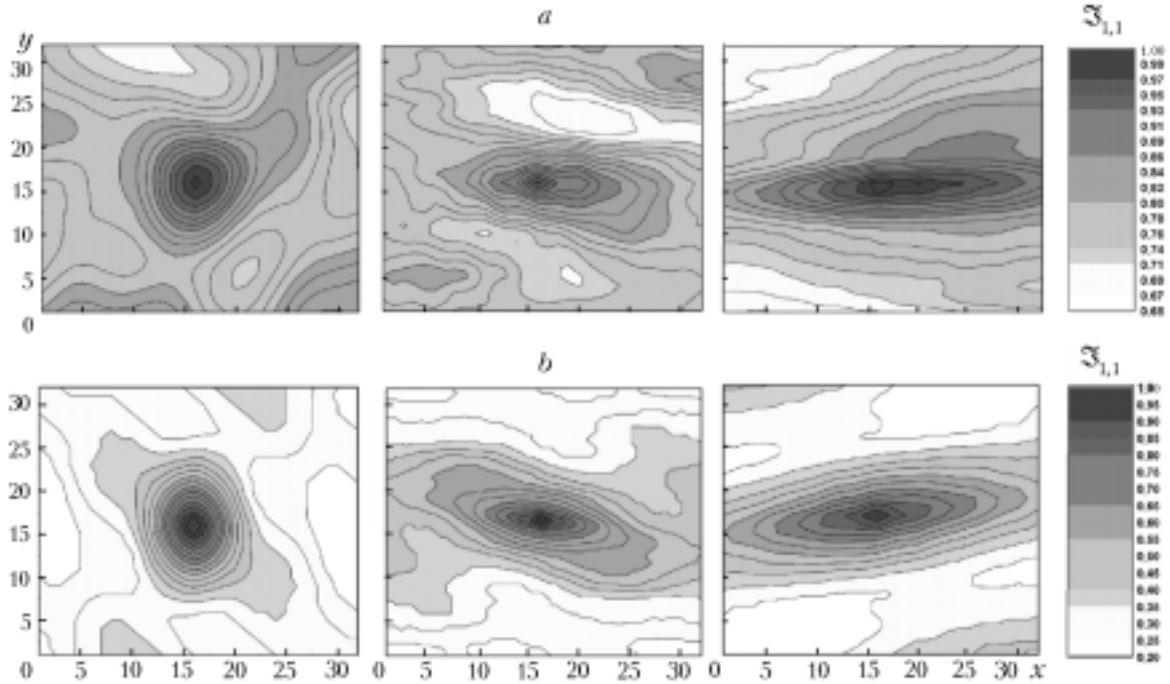

Fig. 6. Cross-sections of the autocorrelation function of a single-exposure specklogram constructed for various rotational velocities of the speckle field generator; a) direct calculation by relation (9); b) calculation with the use of fast Fourier transform by relation (8).

velocity measurements of ~20. This value is very close to the corresponding dynamic range of measurements in the two-exposure PIV technique and speckle photography. For the two-exposure PIV technique this range can easily be adapted to the investigated flow by changing the time between exposures, and for the single-exposure technique — by selecting the dimension of speckles at a "short" exposure $\langle d_\infty \rangle$.

Analysis of the Flow Structure in a Fuel Element. Figure 8 shows fragments of the velocity field in a microchannel of the fuel element model obtained in autocorrelation processing of single-exposure specklograms. The exposure time was adapted to the velocity so that at a maximum velocity in the channel of 5 cm/sec the particle or speckle image had a relative extension of about 5, which corresponds to the linear region of the calibration curve given in Fig. 7. The size of the analyzed region was 20 × 30 mm. In the centered region of the singled-out fragment of size 2 × 2 mm, about 50 velocity vectors with a data density over 10 vectors per 1 mm^2 were obtained. In the

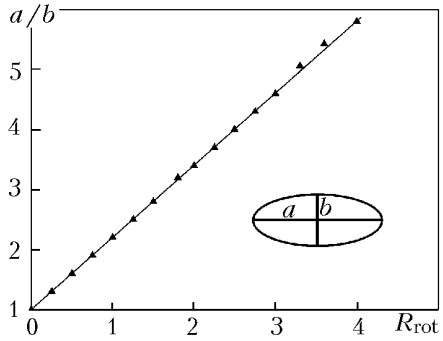

Fig. 7. Results of the single-exposure photograph calibration on a rotating disc made of matte glass (*a/b* — ratio of the semiaxes of the correlation function ellipse).

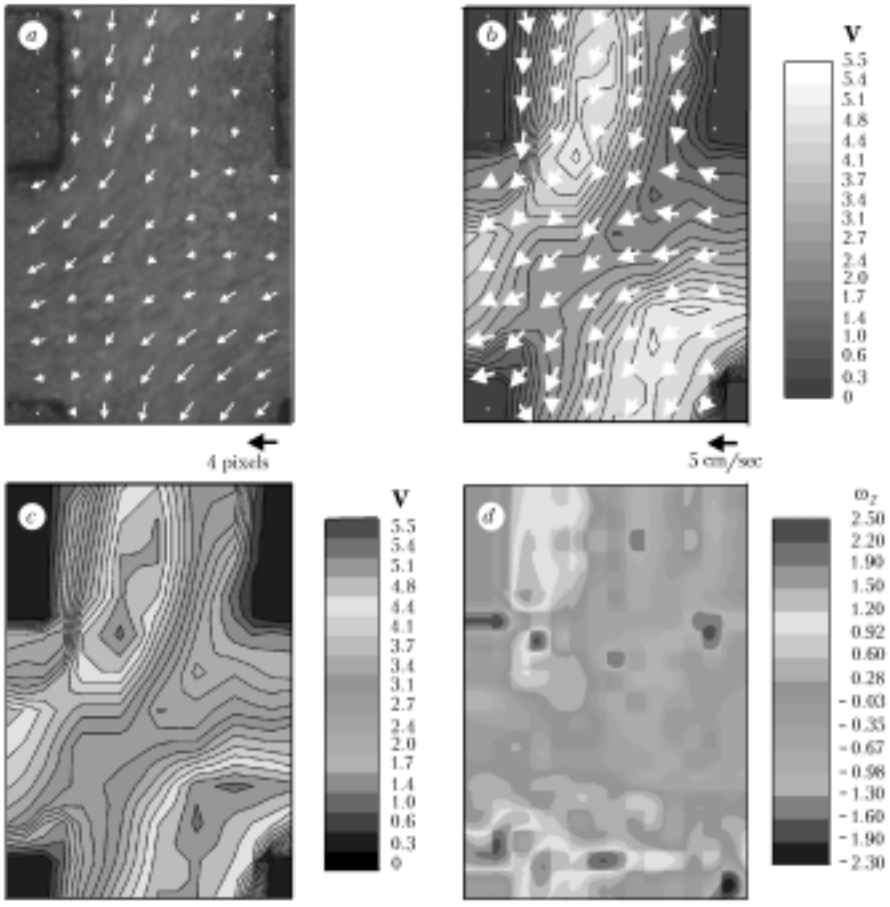

Fig. 8. Specklogram and fragments of the microflow in the fuel cell model reconstructed as a result of digitization of the single-exposure specklogram (a); velocity isolines in the singled-out fragment in a black-and-white representation (b) and in quasi-color (c); field of vorticity z-components (d) calculated in a 20 × 30 mm flow fragment by the data presented in (c). **V**, cm/sec.

flow field on the matrix used at such a data density up to 50,000 velocity vectors can be obtained, which makes it possible to determine with a high accuracy the spatial moments of flow, beginning with vorticity to high-order moments. Figure 8 shows the vorticity field in the singled-out fragment of the flow calculated by the given data. Analysis shows that vorticity is generated mainly in wall-adjacent flows. Despite the fact that in general the vorticity integral

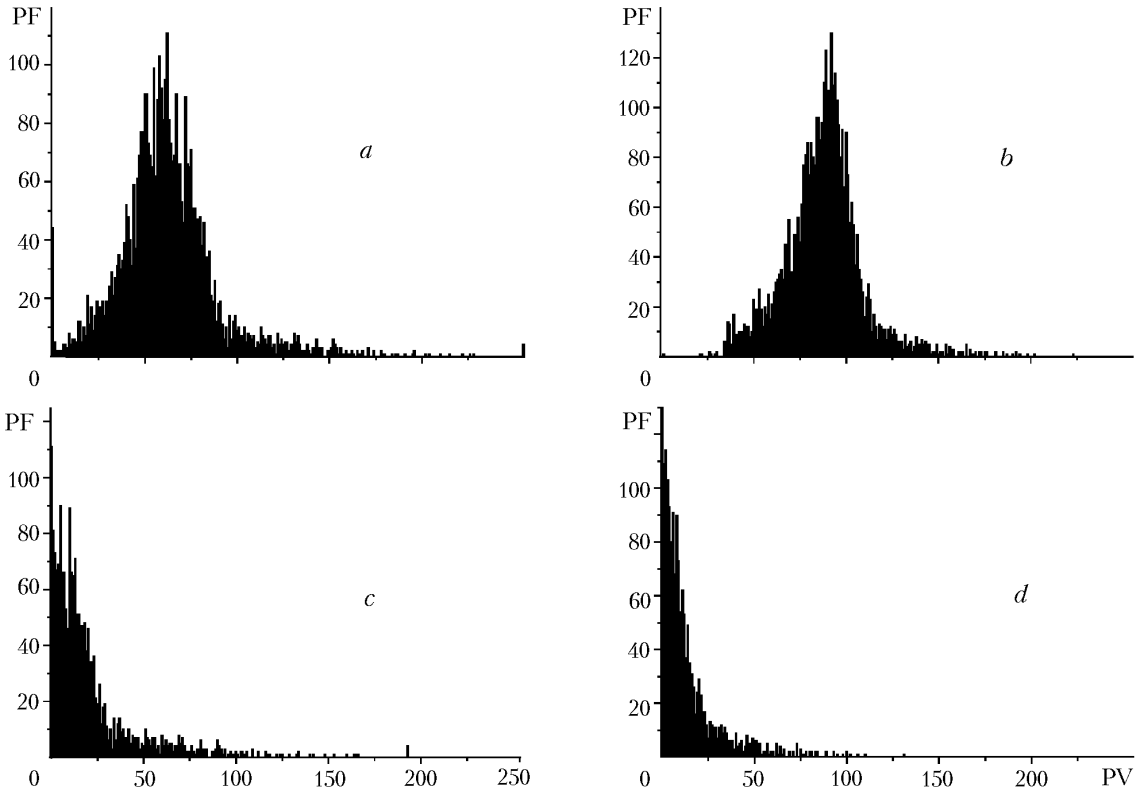

Fig. 9. Probability density of the intensity distribution in the speckle field before (a, b) and after (c, d) filtering of noises: a) and c), statistics for the laser-generated speckle field on a matte plate; b) and d), same for the laser radiation transmitted through a two-meter light guide.

throughout the field is small, the intensity of positive vortices in the singled-out fragment is much higher. The evolution of this quantity in the flow is a convenient parameter characterizing the flow structure and permitting detailed comparison with the results of the numerical simulation of the operating conditions in the PEM fuel element.

Thus, despite the noise organically inherent in them speckle fields are a convenient carrier of useful information extracted from a noisy signal by the methods of statistical processing of two-dimensional arrays. The main sources of speckle noise in the given measuring circuit can be considered to be speckle fields generated by the stationary channel walls and the noises of the CCD structures. These noises soften the initial contrast of the speckle fields and lower the accuracy of anemometry. Additional errors can be introduced by the multiple scattering effects in the presence of a three-dimensional structure of velocity in the microchannel and a high degree of loading of the flow with visualizing particles. One way of controlling the statistics of speckle fields under their filtering is the analysis of the probability density of intensity distribution in the speckle field being filtered proposed in [28]. Taking into account that the probability density in a perfect speckle field is described by a negative exponential dependence on the intensity, in filtering the speckle field its pedestal was subtracted so that the relation

$$P(I) = \frac{1}{\langle I \rangle} \exp\left[-\frac{1}{\langle I \rangle}\right]$$

held. Such filtering is effective for a wide range of optical scheme parameters. It markedly sharpens the field contrast and considerably decreases errors of the above-described processing (see Fig. 9).

In the present paper, we used laser illumination of visualizing particles, which permitted working in the regimes of both speckle field recording and photography of individual particles. In specific cases, incoherent light was used and images of particles were recorded even in "white light" (see, e.g., [45–47]) or with the use of low-coherence laser diodes.

Conclusions. It has been shown that quantitative diagnostics of microflows with the use of digital dynamic speckle photography is possible. The proposed software makes it possible to recover up to 250,000 velocity vectors in a two-dimensional flow region of size 20 × 30 mm in photography with an optical magnification $\mathfrak{M} = 1$. The experiments were performed on a cold model of a fuel cell. Future tests on a hot model will permit real-time optimization of the flow. Investigation of regions of smaller (by a factor of 10–100) sizes is possible with optical magnification by means of adequate microoptics. In the configuration presented, the spatial resolution in the measuring plane is about 100 μm. On the coordinate along the optical beam averaging over the flow depth occurs — in the given case it is 1 mm. The use of tomographic techniques for reconstructing such complex flows proposed in [48, 49] with the aim of obtaining three-dimensional fields is the task of future studies.

The authors wish to thank S. A. Filatov, G. S. Kuchinskii, and A. M. Bratchenya for helping to perform experiments and develop programs for mathematical treatment of images, A. N. Laktyushin for supplying original visualizing microparticles, Prof. J.-B. Solnier and S. A. Martemianov (National Center of Scientific Research, CNRS, France) for useful discussions and recommendations, as well as the INTAS, NAS of Belarus, CNRS of France, and NATO for partial financial support of the work with grants and projects INTAS 03-51-3332, "Vodorod-19", and "Nanotech 1.13".

NOTATION

C_1, C_2, normalizing factors; d, channel width in the fuel element model (see Fig. 2), mm; D, effective waist size (see Fig. 5), mm; D_x, D_y, semiaxes of diffraction halo ellipse, m; D_∞, diffraction halo diameter, m; d_∞, size of speckles upon a "short" exposure, μm; d_{dif}, diameter of the Airy disk of the imaging system mm; d_{p}, visualizing particle diameter, μm; d_{px}, pixel diameter in the CCD matrix, μm; d_{s}, image (speckle) diameter on the recording matrix, μm; $\mathbf{\Delta d}$, displacement vector of speckles, m; Δd_x, Δd_y, extension of speckles in corresponding directions, m; D_{L}, lens diameter, m; F, focal length of the lens, m; $I(m, n)$, laser radiation intensity distribution in the speckle field, W/m^2; I^*, transposed laser radiation intensity distribution in the speckle field, W/m^2; l, channel depth in the fuel element model (see Fig. 2), mm; M, N, dimensions of the broken-up region in statistical treatment; (m, n), current coordinates in the original image; (m^*, n^*), coordinates of the function $\mathbb{R}_{1,2}$ maximum; PF and PV, frequency and intensity of pixels (see Fig. 9); $\mathbf{r}$, z, spatial coordinates, m; R_{rot}, radius vector of a point on a rotating disc (see Fig. 7), cm; $P(I)$, probability density of the speckle field intensity; (p, q), cell number in the CCD matrix; Δt, time interval, sec; T, exposure time, sec; (u, v), current coordinates in the Fourier plane; $\mathbf{V}$, velocity, m/sec; V_x, V_y, velocity components, m/sec; Δ, magnitude of the displacement vector, m; λ, laser radiation wavelength, μm; ρ, wave front curvature, m; $\tilde{\sigma}(m, n)$, experimental noise in the initial intensity of the speckle field, W/m^2; $\sigma(u, v)$, experimental noise in the Fourier plane, W/m^2; σ_{I_1}, rms deviation of the laser radiation intensity in a subregion, W/m^2; τ, time interval, sec; τ_{c}, correlation time, sec; τ_{d}, delay time, sec; ω, current diameter of a laser spot, m; ω_0, laser spot diameter in the waist (in the focus), mm; ω_z, z-component of the vortex for the two-dimensional flow (see Fig. 8d), 1/sec; Ω, solid angle, sr; $\mathbb{C}_{1,1}(m, n)$, speckle field contrast; $\mathbb{F}\{...\}$, Fourier transformation operator; $\mathfrak{J}_{1,1}(m, n)$, autocorrelation function of the speckle field; $\mathfrak{M}$, optical magnification in recording specklograms; $\mathfrak{U}(u, v)$, Fourier image of the speckle field with total intensity; $\mathbb{R}_{1,2}(m, n)$, cross-correlation function of two images. Subscripts: dif, diffraction; c, correlation; d, delay; L, lens; p, particle; px, pixel; rot, rotating, s, speckle; $\langle ... \rangle$, mean value of a quantity.

REFERENCES

1. G. Hoogers, *Fuel Cell Technology Handbook*, CRC Press, Washington DC (2003).
2. *Fuel Cell Handbook* (Sixth Edition). Prepared by EG&G Technical Services, Parsons Inc., and Science Applications International Corporation for the National Energy Technology Laboratory, USA (2002).
3. B. M. Grafov, S. A. Martem'yanov, and L. N. Nekrasov, *Turbulent Diffusion Layer in Electrochemical Systems* [in Russian], Nauka, Moscow (1990).
4. S. A. Grigoriev, S. A. Martemianov, and V. N. Fateev, Electrodiffusion diagnostics of flow regimes in PEM fuel cells, *Magnetohydrodynamics*, **39**, No. 4, 479–485 (2003).

5. Yu. K. Evdokimov and S. A. Martemianov, Continuously distributed sensors for steady-state temperature profile measurements: main principles and numerical algorithm, *Int. J. Heat Mass Transfer*, **47**, 329–340 (2004).
6. W. Hauf and U. Grigull, Optical methods in heat transfer, *Adv. Heat Transfer*, **6**, 133–366 (1970).
7. W. Merzkirch, *Flow Visualization*, 2nd edn., Academic Press, Orlando (1987).
8. N. Fomin, *Speckle Photography for Fluid Mechanics Measurements*, Springer Verlag, Berlin (1998).
9. M. Raffel, C. E. Willert, and J. Kompenhans, *Particle Image Velocimetry: A Practical Guide*, Springer Verlag, Berlin (1998).
10. F. Mayinger and O. Feldman, *Optical Measurements. Techniques and Applications*, 2nd corr. edn., Springer Verlag, Berlin (2002).
11. D. B. Barker and M. E. Fourney, Measuring fluid velocities with speckle patterns, *Opt. Lett.*, **1**, 135–137 (1977).
12. T. D. Dudderar and P. G. Simpkins, Laser speckle photography in a fluid medium, *Nature*, **270**, No. 5632, 45–47 (1977).
13. R. Grousson and S. Mallick, Study of flow pattern in a fluid by scattered laser light, *Appl. Optics*, **16**, No. 9, 2334–2336 (1977).
14. J. P. Lallement, R. Desailly, and C. Froehly, Mesure de vitesse dans un liquide par diffusion coherente, *Acta Astronautica*, **4**, 343–356 (1977).
15. N. A. Fomin, *Speckle Photography of Gas Flows* [in Russian], Nauka i Tekhnika, Minsk (1989).
16. R. J. Adrian, Particle-imaging techniques for experimental fluid mechanics, *Ann. Rev. Fluid Mech.*, **23**, 261–304 (1991).
17. C. E. Willert and M. Gharib, Digital particle image velocimetry, *Exp. Fluids*, **10**, No. 4, 181–193 (1991).
18. W. Merzkirch, T. Mrozewski, and H. Wintrich, Digital particle image velocimetry applied to a natural convective flow, *Acta Mechanika* (Suppl.), **4**, 19–26 (1994).
19. A. Asseban, M. Lallemand, J-B. Saulnier, N. Fomin, E. Lavinskaya, W. Merzkirch, and D. Vitkin, Digital speckle photography and speckle tomography in heat transfer studies, *Optics Laser Technol.*, **32**, 583–592 (2000).
20. N. B. Bazylev, S. M. Vlasenko, E. I. Lavinskaya, and N. A. Fomin, Quasi-real time digital speckle photography of fast processes, *Dokl. Nats. Akad. Nauk Belarusi*, **45**, No. 5, 55–59 (2001).
21. N. Bazylev, N. Fomin, and E. Lavinskaya, Quasi-real time heat transfer characterization by digital dynamic laser speckle photography, in: Bent Sunden and Jurgis Vilemas (Eds.), *Adv. Heat Transfer Eng.*, Begell House Inc. and Lithuanian Energy Institute Press (2003), pp. 767–774 (Proc. 4th Baltic Heat Transfer Conf., Kaunas, Lithuania, August 25–27 2003).
22. N. B. Bazylev, A. M. Bratchenya, E. I. Lavinskaya, S. A. Martem'yanov and N. A. Fomin, Digital laser anemometry of flows in the microchannels of fuel cells of hydrogen power engineering, *Dokl. Nats. Akad. Nauk Belarusi*, **49**, No. 5, 124–129 (2005).
23. J.-J. Kadjo, J.-P. Garnier, J.-P. Maye, S. A. Martemianov, Ch. Coutanceau, Yu. K. Evdokimov, N. B. Bazylev, N. A. Fomin, E. I. Lavinskaya, S. A. Grigoriev, and V. N. Fateev, PEM fuel cell study by multidisciplinary approach, in: N. Fomin, O. Penyazkov, and S. Zhdanok (Eds.), *Physics of Shock Waves, Combustion, Detonation and Non-Equilibrium Processes* [in Russian], Minsk (2005), pp. 79–80.
24. T. S. Durrani and K. A. Greitid, *Laser Systems in Hydrodynamic Measurements* [Russian translation], Énergiya, Moscow (1980).
25. Yu. N. Dubnishchev, B. S. Rinkevichyus, and N. A. Fomin, New methods of laser anemometry in investigations of complex gas-dynamic flows, *Inzh.-Fiz. Zh.*, **76**, No. 6, 3–12 (2003).
26. A. F. Fercher and J. D. Briers, Flow visualization by means of single-exposure speckle photography, *Opt. Commun.*, **37**, 326–329 (1981).
27. J. D. Briers and S. Webster, Quasireal time digital version of single-exposure speckle photography for full-field monitoring of velocity or flow fields, *Opt. Commun.*, **116**, 36–42 (1995).
28. J. D. Briers and S. Webster, Laser speckle contrast analysis (LASCA): a non-scanning, full-field technique for monitoring capillary blood flow, *J. Modern Opt.*, **1**, 174–179 (1996).

29. J. D. Briers, G. Richards, and X. W. He, Capillary blood flow monitoring using laser speckle contrast analysis (LASCA), *J. Biomed. Opt.*, **4**, No. 1, 164–175 (1999).
30. N. B. Bazylev, N. A. Fomin, E. I. Lavinskaya, and S. P. Rubnikovich, Real-time blood micro-circulation analysis in living tissues by dynamic speckle technique, *Acta Bioeng. Biomech.*, **4**, Suppl. 1, 510–511 (2002).
31. N. B. Bazylev, E. I. Lavinskaya, S. A. Naumovich, S. P. Rubnikovich, and N. A. Fomin, Quasi-real time laser probing of biotissues by the methods of dynamic speckle photography, *Dokl. Nats. Akad. Nauk Belarusi*, **47**, No. 4, 46–50 (2003).
32. N. B. Bazylev, E. I. Lavinskaya, and N. A. Fomin, Influence of multiple-scattering processes on the laser probing of biological tissues, *Inzh.-Fiz. Zh.*, **76**, No. 5, 16–24 (2003).
33. L. Gui and W. Merzkirch, A comparative study of the MQD method and several correlation-based PIV evaluation algorithms, *Exp. Fluids*, **28**, No. 1, 36–44 (1999).
34. C. Meinhart, S. Wereley, and J. Santiago, PIV measurements of a microchannel flow, *Exp. Fluids*, **27**, No. 5, 414–419 (1999).
35. C. Meinhart, C. Wereley, and M. Gray, Volume illumination for two-dimensional particle image velocimetry, *Meas. Sci. Technol.*, **11**, No. 6, 809–814 (2000).
36. N. Barakat, H. El-Ghandoor, and A. M. Hamed, Single exposure speckle photography applied to a slow flow field, *Opt. Laser Technol.*, **21**, No. 5, 328–330 (1989).
37. N. A. Fomin, D. Ragozin, H. Wintrich, and W. Merzkirch, Optical speckle patterns generated by turbulent density fields, in: *Proc. Seminar on Optical Methods and Data Processing in Heat and Fluid Flow*, City University Press, London (1992), pp. 211–215.
38. N. A. Fomin, W. Merzkirch, D. Vitkin, and H. Wintrich, Visualization of turbulence anisotropy by single exposure speckle photography, *Exp. Fluids*, **20**, No. 6, 476–479 (1996).
39. C. J. Chen and R. J. Emrich, Investigation of shock tube boundary layer by a tracer method, *Phys. Fluids*, **6**, 1–9 (1963).
40. R. S. Sirohi, Speckle methods in experimental mechanics, *Speckle Metrology*, New York (1993), pp. 99–155.
41. J. D. Briers, Speckle fluctuations as a screening test in the holographic measurements of plant motion, *J. Exper. Bot.*, **29**, 395–399 (1978).
42. A. Oulamara, G. Tribillon, and J. Duvernoy, Biological activity measurement on botanical specimen surfaces using a temporal decorellation effect of laser speckle, *J. Modern Opt.*, **36**, No. 2, 165–179 (1989).
43. A. Hanenkamp and W. Merzkirch, Fourier analysis of the speckle-photographic, density sensitive flow visualization method and application of the "sharp-focusing" effect, *J. Flow Visualization Image Processing*, **12**, 125–136 (2005).
44. T. Asakura and N. Takai, Dynamic laser speckles and their application to velocity measurement of diffuse object, *J. Appl. Phys.*, **25**, 179–194 (1981).
45. E. Bernabeu, J. C. Amare, and M. P. Arroyo, White-light speckle method of measurement of flow velocity distribution, *Appl. Opt.*, **21**, No. 14, 2583–2586 (1982).
46. M. Suzuki, K. Hosoi, S. Toyooka, and M. Kawahashi, White-light speckle method for obtaining an equi-velocity map of a whole flow field, *Exp. Fluids*, **1**, No. 2, 79–81 (1983).
47. M. Grobel and W. Merzkirch, White-light speckle velocimetry applied to plane free convective flow, *Exp. Heat Transfer*, **4**, 253–262 (1991).
48. E. I. Lavinskaya, S. Martem'yanov, J.-B. Solnier, and N. A. Fomin, Limited-projection laser tomography of complex gas-dynamic flows, *Inzh.-Fiz. Zh.*, **77**, No. 5, 94–104 (2004).
49. N. Fomin, E. Lavinskaya, and K. Takayama, Limited projections laser speckle tomography of complex flows, *Opt. Lasers Eng.*, **44**, Nos. 3–4, 335–349 (2006).